JOURNAL OF GEOPHYSICAL RESEARCH, VOL. 111, A11S02, doi:10.1029/2005JA011351, 2006

Click Here for Full Article

Observations and modeling of energetic electron dynamics during the October 2001 storm

Y. S. Miyoshi,[1] V. K. Jordanova,[2] A. Morioka,[3] M. F. Thomsen,[2] G. D. Reeves,[2] D. S. Evans,[4] and J. C. Green[4]

Received 4 August 2005; revised 17 November 2005; accepted 3 January 2006; published 21 September 2006.

[1] We examined and simulated the dynamics of energetic electrons during the October 2001 magnetic storm with the relativistic RAM electron model for a wide range of energies. The storm had a rapid main phase followed by a day of strong geomagnetic activity that produced a second *Dst* minimum and then a very quiet recovery phase. During the main phase and the period of intense activity, the observed hot electron flux (E = 30 keV) increased at low L while decreasing at large L and then decayed abruptly at the beginning of the recovery phase when activity subsided. The flux of subrelativistic (E = 100–300 keV) electrons also increased at low L and decreased at large L during the main phase and the period of intense activity but remained high throughout the recovery phase. In contrast, the relativistic (E = 300–1200 keV) electron flux decreased during the main phase, remained low throughout the period of intense activity, and then increased above prestorm values during the recovery phase in spite of the low activity. The highest energy electron flux (E > 1200 keV) decreased during the main phase and never recovered to prestorm levels. The numerical simulation was compared with observations. We identified the physical processes which produce the flux variations at the different energies. In the simulation, the hot electrons were convected inward during the main phase, reproducing the observed local time flux asymmetry. The higher-energy electrons, on the other hand, were predominantly transported inward by radial diffusion and not convective motion. The simulation was not able to reproduce the subrelativistic and relativistic electron flux enhancement and spatial expansion as observed during the recovery phase. In the simulation, most of the energization occurred around the main phase and the period of intense activity with negligible transport or flux enhancement during the recovery phase. The discrepancy between the observed and simulated high energy electron flux suggests that only convective transport and radial diffusion cannot fully explain the electron dynamics. An additional mechanism may be necessary to explain enhancements of high energy electron flux during the recovery phase of the storm.

Citation: Miyoshi, Y. S., V. K. Jordanova, A. Morioka, M. F. Thomsen, G. D. Reeves, D. S. Evans, and J. C. Green (2006), Observations and modeling of energetic electron dynamics during the October 2001 storm, *J. Geophys. Res.*, *111*, A11S02, doi:10.1029/2005JA011351.

1. Introduction

[2] The dynamics of the terrestrial energetic electrons in the ring current/radiation belts have been studied for an extensive time period (see *Friedel et al.* [2002] for review). The classic picture considered radial diffusion from an outer magnetospheric source to be the major mechanism for accelerating radiation belt particles. However, recent studies suggest that internal acceleration mechanisms, which locally accelerate electrons, may also contribute [e.g., *Summers et al.*, 1998; *Brautigam and Albert*, 2000; *Selesnick and Blake*, 2000; *Obara et al.*, 2001; *Miyoshi et al.*, 2003; *Green and Kivelson*, 2004]. In fact, both processes may ultimately be important for producing particle acceleration and flux increases [*O'Brien et al.*, 2003]. Discerning which mechanisms produce flux variations is challenging because satellite observations are often restricted to single point measurements, incomplete time resolution, or sampling only limited L shell. Therefore comparing observations with comprehensive models that include several physical processes is necessary to clarify the responsible processes for the dynamics of the inner magnetosphere.

[3] The equilibrium structure of high energy electrons including the slot region can be well modeled by both

[1]Solar-Terrestrial Environment Laboratory, Nagoya University, Nagoya, Japan.
[2]Los Alamos National Laboratory, Los Alamos, New Mexico, USA.
[3]Planetary Plasma and Atmospheric Research Center, Tohoku University, Sendai, Japan.
[4]NOAA, Boulder, Colorado, USA.

Copyright 2006 by the American Geophysical Union.
0148-0227/06/2005JA011351$09.00

one-dimensional (1-D) [*Lyons and Thorne*, 1973] and three-dimensional models (Salammbo) [*Beutier and Boscher*, 1995]. However, it is difficult to model that the dynamics of energetic electrons during geomagnetic disturbances includes complicated processes. Several dynamical physical models that calculate time variations of the radiation belts have been developed with 1-D and 3-D radial diffusion and 4-D convective-diffusion codes. Some of these models have been used to qualitatively define the evolution of the radiation belts under different conditions but were not directly compared to data or did not explicitly consider dynamic storm times. For example, *Selesnick et al.* [1997] developed a 1-D Fokker-Planck diffusion model and used it to examine evolution and decay of the phase space density during quiet geomagnetic conditions. In their later study, *Selesnick and Blake* [2000] used the same diffusion model to show the expected evolution of phase space density profiles for two different scenarios: diffusion from an external source at large L into the inner magnetosphere and diffusion from an internal source at low L. *Bourdarie et al.* [1997] developed a 4-D convective-diffusion model and examined the response of the radiation belts to a sudden flux enhancement at the outer boundary. More recently, *Shprits and Thorne* [2004] examined how different lifetimes and boundary conditions could affect radiation belt evolution using a 1-D Fokker-Planck equation.

[4] Other studies did focus on modeling specific storm periods and comparing with observations. For example, *Brautigam and Albert* [2000] performed a numerical simulation of the 9 October 1990 storm using a 1-D Fokker-Planck equation in the region of L = 3.5–6.6. They used time-dependent radial diffusion coefficients parameterized by the *Kp* index and time-dependent boundary conditions. They compared the simulation results with phase space density profiles derived from CRRES observations and found that radial diffusion alone is not sufficient to explain the observed negative phase space density gradients of high M (magnetic moment) electrons. *Miyoshi et al.* [2003] solved a 1-D Fokker-Planck equation for the 3 November 1993 storm, using the time-dependent radial diffusion coefficients of *Brautigam and Albert* [2000] as well as realistic loss processes due to both Coulomb collisions and wave-particle interactions. This radial diffusion model showed the energy spectrum hardening first at large L contrary to observations, suggesting that internal acceleration mechanisms should be included to explain flux variations during storms. Later, *Miyoshi et al.* [2004] extended the 1-D radial diffusion simulation from L = 1.0 to L = 6.6 and qualitatively reproduced the long-term variations over two solar cycles indicating that radial diffusion may be important for defining some of the long-term and global features of the radiation belts, while internal acceleration is necessary to reproduce storm time flux increases. *Li et al.* [2001] and *Li* [2004] developed a 1-D radial diffusion model from L = 4.5–11.0 with fixed boundary conditions. They developed empirical radial diffusion coefficients that varied as a function of solar wind speed and IMF and included both the *Dst* effect and solar wind dynamic pressure effects that can cause flux decreases. They compared the model to daily flux measurements at geosynchronous orbit and successfully reproduced the long-term flux variations. *Zheng et al.* [2003] developed a 4-D convective-diffusion model for relativistic electrons in a nondipolar field and modeled the 12 August 2000 storm using the radial diffusion coefficient of *Li et al.* [2001] and successfully reproduced flux variations observed at geosynchronous orbit throughout the storm.

[5] Besides these radial diffusion and/or convective-diffusion calculations, there are several other approaches for simulating energetic particle behavior in the inner magnetosphere. *Liu et al.* [2003] did a phase space mapping simulation of the 26 August and 10 October 1990 storms. They considered how impulsive fluctuations of the polar cap potential would affect diffusive transport of higher energy electrons. They found that ~150 keV electron flux increased at $L \sim 3.5-5$ if they included the effects of fluctuations of the cross polar cap potential. However, the model could not produce an increase of $E > 200$ keV electron flux at $L \sim 3.5-5$ suggesting the need for local acceleration together with adiabatic radial transport. *Elkington et al.* [2004] calculated trajectories of relativistic electrons in MHD fields that should include both ambient potential field fluctuations and ULF pulsations. They showed that MeV electrons can, at least theoretically, be transported earthward from the plasma sheet and be trapped at $L = 3$. In addition to these simulation efforts, *Naehr and Toffoletto* [2005] used data assimilation to understand the dynamics of the radiation belts comprehensively from satellite data.

[6] In this study, we show particle observations from several satellites during the October 2001 magnetic storm which was selected for study by the Geospace Environment Modeling/Inner Magnetosphere and Storms (GEM/IMS) campaign. Observations of ring current/radiation belt electrons from several LANL satellites at geosynchronous orbit and low-altitude satellites NOAA-15 and 16, and the Polar satellite are presented in section 2. We then simulate the evolution of ring current/radiation belt electron flux with the newly developed relativistic ring current-atmosphere interaction model (RAM) [*Jordanova and Miyoshi*, 2005] and compare the model output with the observations in order to examine the physical processes which control flux variations at different energies. The RAM model calculates distribution functions of equatorial and off-equatorial particles with a wide range of energies from a few hundred eV to a few MeV. A detailed description of the model is given in section 3. In section 4, we compare the temporal and spatial evolution of the ring current and relativistic electrons. A summary of the results is given in section 5.

2. Observations

2.1. Interplanetary Medium

[7] The interplanetary medium of the October 2001 storm was monitored by ACE. Figure 1 shows the ACE measurements for a 4-day period from DOY 294 (21 October) to 297 (24 October), 2001 along with polar cap potential, *AE*, *Kp*, and *Dst* indices. Here, the polar cap potential was derived from the PC index [*Troshichev et al.*, 1988] using the empirical equation of *Troshichev et al.* [1996]. At 1600 UT on 294, an interplanetary shock arrived. The amplitude of the IMF Bz component was about -20 nT, and the bulk speed of the solar wind reached 700 km/s. The *Dst* index indicated a storm commencement and subsequent evolution of a strong storm main phase. The storm main phase was followed by a day of intense activity where *Dst* remained low and then

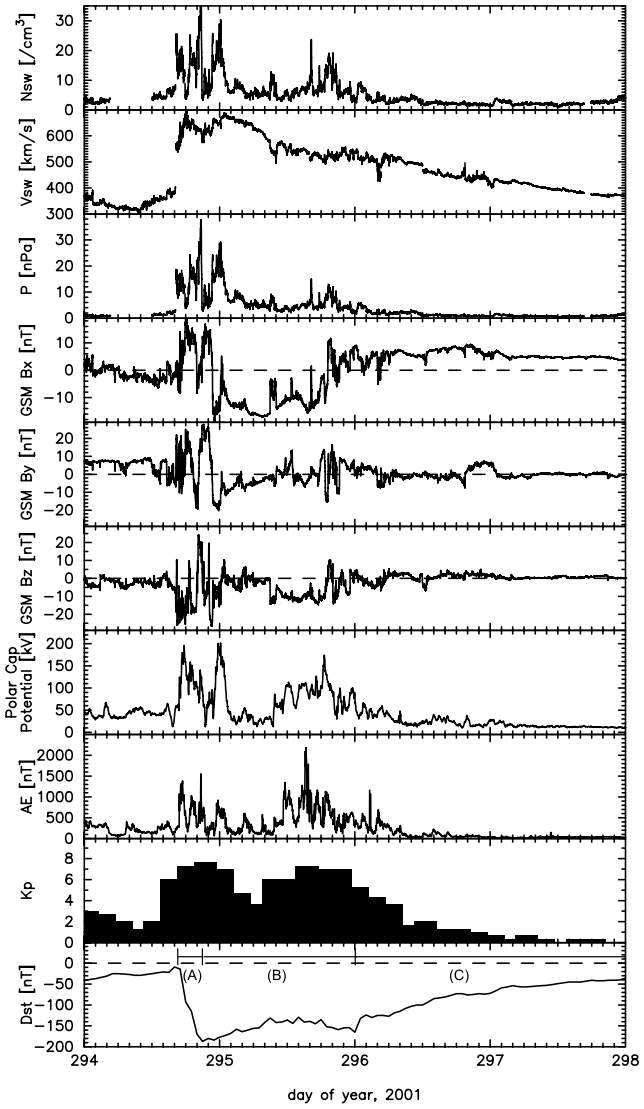

Figure 1. Solar wind and IMF in GSM coordinates from the ACE satellite along with the polar cap potential, *AE* index, *Kp* index, and *Dst* index for the interval of DOY 294 to 297, 2001. Labels A, B, and C indicate main phase, intense activity period, and recovery phase respectively.

decreased slightly to a second minimum value. The *Kp* and *AE* indices reached a maximum of 8- at 2200 UT and about 1400 nT at 1700 UT on 294, respectively. The first minimum *Dst* index was −187 nT at 2200 UT. Following the first shock arrival, at 0900 UT on 295, the second negative excursion of IMF Bz occurred with amplitude of −15 nT. During this time, *Kp* and *AE* again reached maxima of 7+ at 1600 UT and about 2100 nT at 1500 UT on 295, respectively. The second minimum *Dst* of −165 nT was recorded at 0100 UT on 296. Thus the total duration of strong geomagnetic activity was quite long; about 32 hours. The second minimum of the *Dst* index was a little bit smaller than the first, while the maximum *AE* index was greater than the first.

[8] After a positive excursion of the IMF Bz component at ∼0600 UT on 296, the amplitude of Bz was almost 0. The polar cap potential was below 20 kV, and the *AE* index indicated the absence of any substorm activity during the recovery phase. It is interesting that the amplitude of By was also 0 after 297 (24 October), and therefore the IMF had only a positive Bx component. The *Dst* index showed a slow storm recovery lasting several days. Therefore the October 2001 magnetic storm had a contrastive nature: a rapid main phase (period A in Figure 1) followed by a period of intense activity with the second *Dst* minimum (period B), and then a quiet and slow recovery phase (period C).

2.2. LANL Observations

[9] Figure 2 shows the density of 0.03 to 45.0 keV electrons measured by the MPA instrument on board five LANL satellites (1990−095, 1991−080, 1994−084, LANL-97A, LANL-01A). The vertical dotted lines in each panel indicate local midnight. It should be noted that the LANL satellites were in the magnetosheath when the strong density enhancement was observed at the noonside. During the main phase, the electron density increased up to 2−3/cm^3, typical of the so-called superdense plasma sheet [*Borovsky et al.*, 1997]. Near the second *Dst* minimum, the electron density was enhanced at geosynchronous orbit and sometimes reached over 2/cm^3, but the duration time of the enhanced flux was shorter than during the first *Dst* minimum.

[10] Figure 3 shows the energetic electron flux from 50 keV to 1350 keV measured by the SOPA instrument

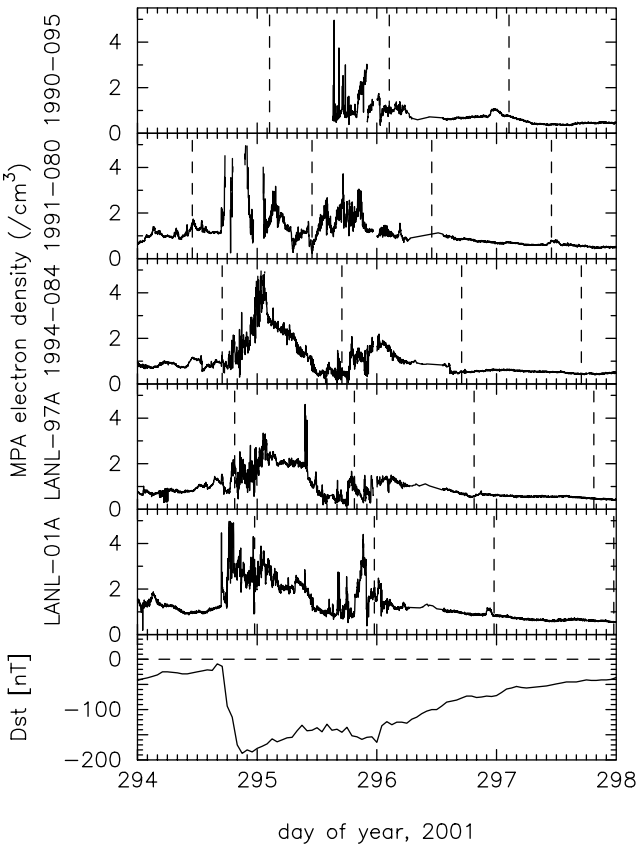

Figure 2. Electron density (0.03−45.01 keV) measured by the MPA instruments on board the LANL satellites; 1990−095, 1991−080, 1994−084, LANL-97A and LANL-01A. The vertical line of each panel indicates local midnight of each satellite.

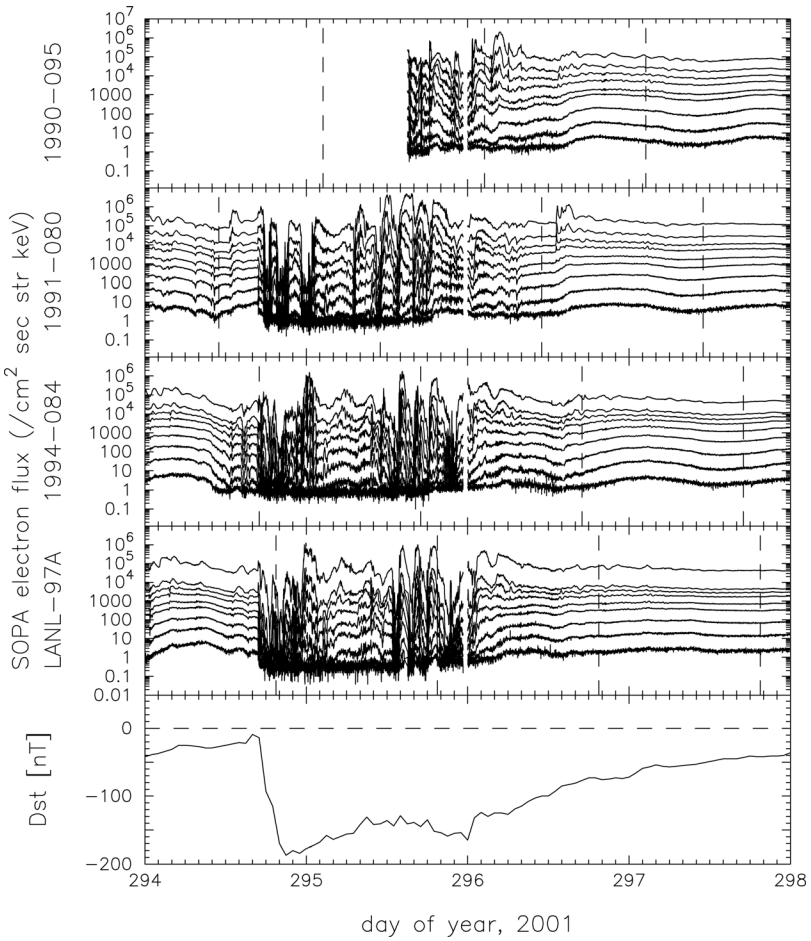

Figure 3. Energetic electron flux measured by SOPA from LANL satellites 1990–095, 1991–080, 1994–084, and LANL-97A. The vertical dotted line of each panel indicates local midnight. The nine traces correspond to each energy; 50–75 keV, 75–105 keV, 105–150 keV, 150–225 keV, 225–315 keV, 315–500 keV, 500–750 keV, 750–1100 keV, and 1100–1500 keV, respectively.

of the same LANL satellites except for LANL-01A. After the storm commencement, the energetic electrons at geosynchronous orbit showed a large flux dropout at all energies. There were several injections at geosynchronous orbit related to substorms on DOY 295, which caused the flux at the lower energies to increase. These flux enhancements at substorm onsets were not always related to low energy electron density enhancements as shown in Figure 2. During the recovery phase, the flux of higher energy electrons increased gradually without any injection signature and recovered to the prestorm level at DOY 297.

2.3. NOAA-15 and 16 Observations

[11] During the storm, the NOAA-15 and 16 satellites continuously observed hot (E = 30–100 keV), subrelativistic (E = 100–300 keV), and relativistic (E = 300–2500 keV) electrons. The altitudes of NOAA 15 and 16 are 827 km and 855 km, respectively. The local times of the ascending and descending node of NOAA-15 were 1930 (dusk) and 0730 (dawn), and the local times of NOAA-16 were 1400 (noon) and 0200 (night). The satellites carry a pair of solid-state MEPED detector telescopes. The first views radially outward along the Earth satellite vector (0 deg telescope) and the second (90 deg telescope) views in a direction perpendicular to the first telescope [*Evans and Greer*, 2000]. The 90 deg telescope has been oriented to view antiparallel to the satellite velocity vector and corresponded to trapped particles at high latitudes and particles with local pitch angle $\alpha \leq 60^\circ$ at low latitudes. As shown in Figure 4d, the corresponding equatorial pitch angle was $\leq 18^\circ$ at L = 2. For this reason, at low latitude with $L \leq 2.0$ the 90 deg telescope observed particles inside the local atmospheric loss cone and the count rate was very low. Therefore the MEPED data at $L \leq 2.0$ was not discussed in this study. The MEPED instrument observed electrons at three different energies: 30–2500 keV, 100–2500 keV, and 300–2500 keV. In this study we obtained the flux of 30–100 keV and 100–300 keV electrons by subtracting the count rate of the 100–2500 keV channel from that of 30–2500 keV channel and that of 300–2500 keV from that of 100–2500 keV. In order to avoid the effect of the South Atlantic Anomaly, the NOAA data from only the northern hemisphere are used.

[12] Figure 4 is an L-time diagram of energetic electrons obtained from the 90 deg sensor. Here, L is McIlwain L value derived from the IGRF model. It should be noted that the periodic modulation in the lower L shell reflects the well-known variation of trapped particle fluxes with geographic longitude when observed at a constant low altitude

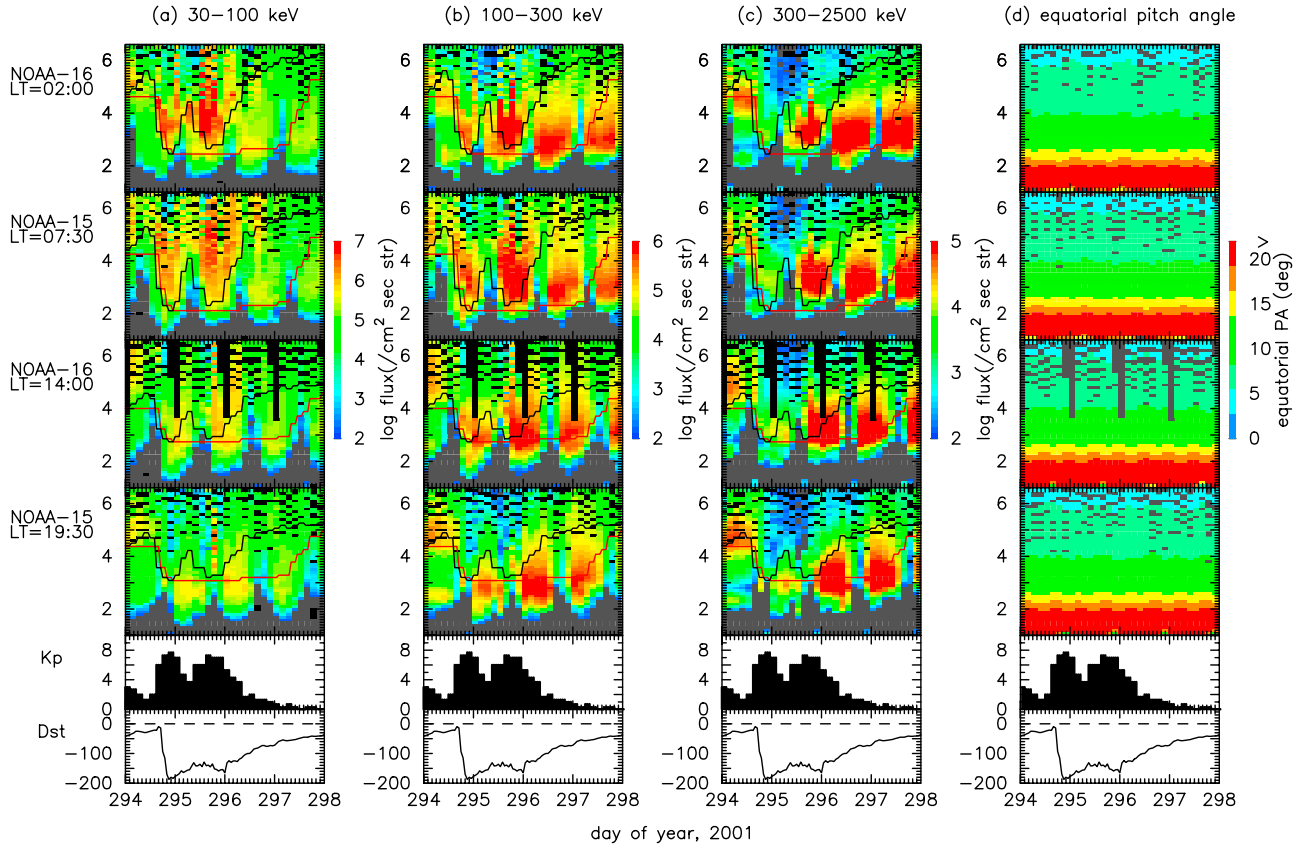

Figure 4. *L*-time diagram of integral electron flux measured by NOAA satellites. (a) 30–100 keV electron, (b) 100–300 keV electron, (c) 300–2500 keV electron, and (d) corresponding equatorial pitch angle. From top to bottom, LT of 0200 (NOAA-16), LT of 0730 (NOAA-15), LT of 1400 (NOAA-16) and LT of 1930 (NOAA-15). Black areas in the plot correspond to the missing data period.

that arises because of the longitudinal variation in Earth's magnetic field strength [*Berg and Søraas*, 1972]. Figure 4d indicates the corresponding equatorial pitch angle calculated from the IGRF model. From top to bottom, the diagram shows the flux distribution at LT 0200 (night), 0730 (dawn), 1400 (noon), and 1930 (dusk), respectively. The red line of each panel is the empirical plasmapause location as a function of the *Kp* index [*O'Brien and Moldwin*, 2003], taking into consideration the MLT dependence. The black line is also derived from the same equation of the empirical plasmapause, where the refilling time of the plasmasphere is not considered. Therefore the black line can be used as a proxy for changes in magnetospheric convection.

[13] Figure 4a shows the 30–100 keV electron flux. During the main phase, intense enhancements of 30 keV electrons were observed at L = 2.5–5 at night and dawn, while the flux remained low around L = 6. On the other hand, the enhancement seemed to be weak at noon and dusk demonstrating a clear local time asymmetry at these low energies. At dusk, a flux enhancement was observed in a restricted region of L = 2.5–3.0, which is likely a result of electrons drifting from dawn due to magnetic drift. During the recovery phase no flux enhancements occur possibly due to weak convection and the absence of substorm activity. Electron fluxes at 30 keV around L = 3 remained low throughout the recovery phase.

[14] Figure 4b shows the 100–300 keV electron flux. Typically, electrons of this energy vary in a manner similar to both the hot electrons (E < 100 keV) and relativistic electrons (E > 300 keV). Before the storm commencement, the radiation belts had a typical structure with an inner and outer belt separated by the slot region near L = 3. At the storm main phase, the flux at all local times decreased in the outer region (L > 5). The electron flux increased around L = 3–5 at night and dawn and in a more limited area around L = 3–4 at noon and dusk. The flux enhancement during the second *Dst* minimum was much larger than that of the first one. In the recovery phase, the flux remained high in the L-value interval of 2.5–4.0.

[15] Figure 4c shows the 300–2500 keV electron flux. After the storm commencement, the flux of the outer belt at L > 4 disappeared suddenly. During the second *Dst* minimum, the flux around L = 3.5 rapidly increased at all local times. The local time asymmetry of the flux enhancement, which appeared at 30–100 keV and 100–300 keV, seemed not to be significant at this higher energy. During the recovery phase, the flux enhancement region expanded outward in L. The flux recovery and enhancement continued throughout the recovery phase similar to what was observed at geosynchronous orbit.

2.4. Polar Observations

[16] During this storm, the Polar satellite successively observed the inner magnetosphere. The orbit of the satellite

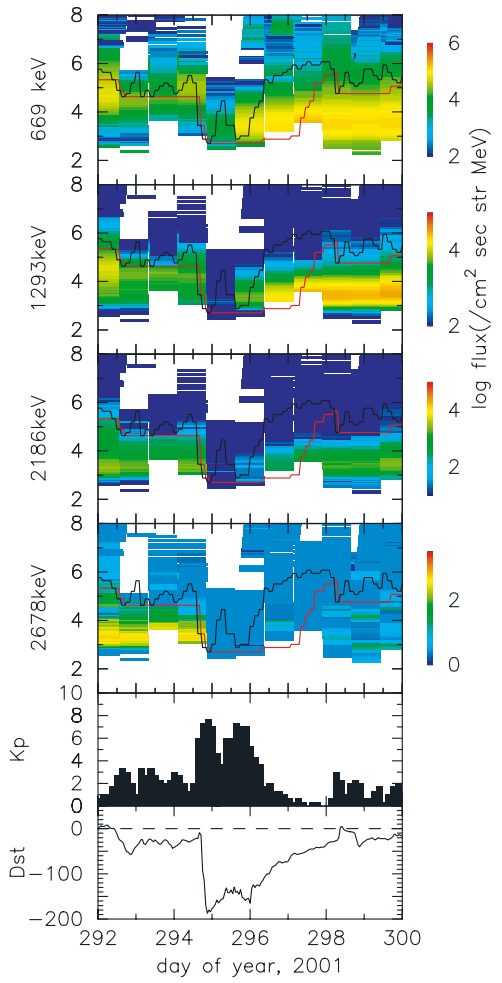

Figure 5. *L*-time diagram of relativistic electron flux measured by the Polar satellite. White areas in the plot correspond to the missing data period.

was in the noon-midnight meridian and the apogee was in the night side during the period. The electron fluxes used in this study were obtained from the HIST instrument [*Blake et al.*, 1995]. The HIST instrument measured relativistic electron fluxes at energies between 700 and 7000 keV. The instrument calibration is described by *Selesnick and Blake* [2000].

[17] Figure 5 is an *L*-time diagram showing the flux of 90 deg pitch angle electrons at several energies measured by Polar/HIST. These data were obtained at ~5000 km around the perigee of the orbit. From 669 keV to 1293 keV, the flux variation of the outer belt showed similar variation to the NOAA 300–2500 keV flux variation. That is, the flux of the outer belt decreased after commencement of the main phase and then increased first around $L = 3.5$ expanding gradually outward throughout the recovery phase. The higher-energy electron flux (1604–2186 keV) decreased during the main phase and took longer times to recover than the low-energy electron flux. The flux of these energies recovered to, but never increased more than, the prestorm level. The 2678 keV electron flux decreased after the main phase and never recovered to the prestorm level. Therefore the maximum energy, which showed a flux increase above the prestorm level, was about 1200 keV. The electron flux enhancement was substantially larger at lower energies than at higher energies. It is interesting that the relativistic electron flux below about 1200 keV increased gradually in the outer belt during the recovery phase even though the magnetic activity was very quiet and there were no substorms.

3. Model Description

[18] In this study we simulate the time evolution of energetic electron distribution functions during the October 2001 magnetic storm with the relativistic RAM model [*Jordanova and Miyoshi*, 2005]. The RAM model can calculate 4-D particle distribution as a function of *L*, MLT, energy, and pitch angle [*Jordanova et al.*, 1997, 2001]. We solve numerically the bounce averaged relativistic Boltzmann equation of the distribution function $Q_e(R_0, \phi, E, \mu_0, t)$ for electrons:

$$\frac{\partial Q_e}{\partial t} + \frac{1}{R_0^2}\frac{\partial}{\partial R_0}\left(R_0^2\left\langle\frac{dR_0}{dt}\right\rangle Q_e\right) + \frac{\partial}{\partial \phi}\left(\left\langle\frac{d\phi}{dt}\right\rangle Q_e\right) + \frac{1}{\gamma p}\frac{\partial}{\partial E} \times \left(\gamma p\left\langle\frac{dE}{dt}\right\rangle Q_e\right) + \frac{1}{h(\mu_0)\mu_0}\frac{\partial}{\partial \mu_0}\left(h(\mu_0)\mu_0\left\langle\frac{d\mu_0}{dt}\right\rangle Q_e\right) = \left\langle\left(\frac{\partial Q_e}{\partial t}\right)_{rd}\right\rangle + \left\langle\left(\frac{\partial Q_e}{\partial t}\right)_{loss}\right\rangle \quad (1)$$

Here p is the relativistic momentum and γ is the relativistic factor defined by $\gamma = 1 + E/m_0 c^2$ where m_0 is the electron rest mass, c is speed of light, and E is the kinetic energy: 500 eV to 3700 keV. The radial distance in the equatorial plane R_0 is from 2 R_E (Earth radii) to 6.5 R_E, ϕ is the geomagnetic east longitude, and μ_0 is the cosine of the equatorial pitch angle from 0 to 1. See *Jordanova and Miyoshi* [2005] for detailed description of the terms in the left-hand side. The first term in the right-hand side indicates radial diffusion and the second term indicates several loss processes. In the present study, the second term incorporates Coulomb collisions including both pitch angle scattering and energy degradation, wave-particle interactions, and electron precipitation into the atmosphere.

$$\left\langle\left(\frac{\partial Q_e}{\partial t}\right)_{loss}\right\rangle = \left\langle\left(\frac{\partial Q_e}{\partial t}\right)_{cc}\right\rangle + \left\langle\left(\frac{\partial Q_e}{\partial t}\right)_{wp}\right\rangle + \left\langle\left(\frac{\partial Q_e}{\partial t}\right)_{atm}\right\rangle \quad (2)$$

The loss cone corresponds to an altitude of 200 km. In the model, the geomagnetic field is assumed to be a dipole, and the Volland-Stern electric field [*Volland*, 1973; *Stern*, 1973] with the Maynard-Chen potential [*Maynard and Chen*, 1975] is used. The shielding factor of the Volland-Stern electric field is 2, and the amplitude of electric potential is changed as a function of the *Kp* index. The RAM model is coupled to the time-dependent plasmasphere model [*Rasmussen et al.*, 1993], which solves the temporal evolution of plasmaspheric electron density, and the following composition of thermal ions is assumed: 77% H+, 20% He+, and 3% O+. The calculated thermal plasma densities are used to calculate losses due to Coulomb collisions and also to determine the plasmapause location at which the characteristics of plasma waves drastically change.

3.1. Radial Diffusion

[19] The relativistic electrons hardly move in the radial direction because of strong magnetic drift. Thus radial diffusion has been considered as the primary transport mode of relativistic electrons [e.g., *Lyons and Schulz*, 1989]. The relativistic RAM model calculates diffusive transport in equation (1) using the following Fokker-Planck equation,

$$\left\langle \left(\frac{\partial Q_e}{\partial t}\right)_{rd} \right\rangle = R_0^2 \frac{\partial}{\partial R_0}\left(\frac{\langle D_{R_0R_0}\rangle}{R_0^2}\frac{\partial Q_e}{\partial R_0}\right)_{(M,J)} \tag{3}$$

where $D_{R_0R_0} = R_E^2 D_{LL}$ is the radial diffusion coefficient, M is the first adiabatic invariant and J is the second adiabatic invariant. In this study, we adopt the empirical function of *Brautigam and Albert* [2000] for the rate of radial diffusion D_{LL} considering only magnetic diffusion. Because the diffusion coefficient of *Brautigam and Albert* [2000] is only defined for $Kp < 6$, we used the diffusion coefficient of $Kp = 6$ as the maximum value. This may result in the underestimation of fluxes during the main phase and the period of intense activity, because the Kp index during the period often became greater than 6. The pitch angle dependence of the radial diffusion coefficient is considered in this study using the following formula [*Schulz*, 1991],

$$D_{LL}^m \propto D_0^m L^{10}\left(\frac{Q(y)}{180D(y)}\right)^2 \tag{4}$$

where y is sine of pitch angle, and $Q(y)$ and $D(y)$ is the auxiliary function. The equation indicates that particles with small pitch angles have small radial diffusion coefficients. With all the contributing terms, the relativistic RAM model can simulate the convection dominated low energy particles, the diffusion dominated high-energy particles, and the medium energy range in which both processes could be effective.

3.2. Wave-Particle Interactions

[20] It is believed that electron loss due to wave-particle interactions plays an important role in the evolution of ring current/radiation belt electrons. In this model, the wave-particle interactions both inside and outside plasmapause are considered. The flux decrease due to pitch angle scattering can be calculated with the following equation for all pitch angles,

$$\left(\frac{\partial Q_e}{\partial t}\right)_{wp} = -\frac{Q_e}{\tau_{wp}} \tag{5}$$

where τ_{wp} is the lifetime of wave-particle interactions. Inside the plasmapause, we use the electron lifetimes calculated by *Albert* [1999] based on pitch angle scattering by whistler mode hiss, lightning whistler, and VLF transmitters [*Abel and Thorne*, 1998]. Outside the plasmasphere, we use strong pitch angle diffusion for electrons below a critical energy E_c and pitch angle scattering by plasma waves for electrons above E_c. Referring to *Liu et al.* [2003], we use the critical energy of 2 keV. The lifetime in the case of strong diffusion is determined from *Lyons and Williams* [1984] as function of energy and loss cone angle. For electrons with energy above E_c, wave-particle interactions with whistler mode chorus is considered, and the empirical lifetimes of *Chen and Schulz* [2001] which vary as a function of L and energy are used.

[21] As shown in observational studies [*Meredith et al.*, 2001, 2004], the distribution of whistler mode waves in the inner magnetosphere changes drastically with magnetic activity and depends on local time. Recently, *Horne et al.* [2005] showed theoretically that diffusion coefficients of wave-particle interactions vary with magnetic local time and latitude. As shown by *Shprits and Thorne* [2004], time variations of lifetimes outside the plasmasphere may affect the spatial evolution of the outer belt. Moreover, *Shprits et al.* [2005] did a 1-D radial diffusion simulation and compared with the CRRES data. They concluded that the electron life times due to the wave-particle interactions outside plasmasphere are much shorter than the life times due to plasmaspheric hiss and Coulomb scattering. The wave distribution used in the present study, however, is assumed to have a simple form. For the lifetime of electrons outside the plasmasphere with energy above E_c, the following simple relationship is used for $Kp \leq 6$, and we use the life time of $Kp = 6$ as the maximum value

$$\tau_{wp}(Kp) = \tau_{wp}(Kp = 0) \times (1.0 - 0.15Kp) \tag{6}$$

where the lifetimes of wave-particle interactions are independent of local times.

3.3. Initial and Boundary Conditions

[22] In the present study the electron distribution functions during magnetically quiet periods from HYDRA of Polar [*Scudder et al.*, 1995] are used as an initial condition below 10 keV, and the empirical AE8/MAX model [*Vette*, 1991] is used for higher-energy electrons. It is assumed that the pitch angle distributions are isotropic and the particle distributions are symmetric in the magnetic local time.

[23] The flux at the outer boundary of the simulation ($R_0 = 6.5\ R_E$) is derived from the MPA and SOPA measurements of LANL satellites. In this simulation, the outer boundary conditions are updated every 2 hours. Therefore the time variation and local time dependence of flux at geosynchronous orbit is included. The pitch angle distribution at the boundary is kept isotropic throughout the simulation.

4. Simulation Results and Discussions

[24] In this section we examine the temporal and spatial evolution of the simulated ring current and relativistic electrons from DOY 294 to 298 and compare with the satellite observations. Figure 6 is an L-time diagram of the RAM simulated electrons with energies of 30 keV, 110 keV, and 290 keV and 20 deg pitch angle at the magnetic equator. It should be noted that in Figure 6 we plot differential flux, while NOAA satellites measures integral flux (Figure 4). The electrons measured by NOAA and Polar have variable pitch angles. Particularly, the average equatorial pitch angle of the electrons measured by the NOAA MEPED sensor is about 10–20 deg as shown in Figure 4. Note that the L-time diagram from the RAM model is derived from the dipole field while that of the observations is derived from IGRF.

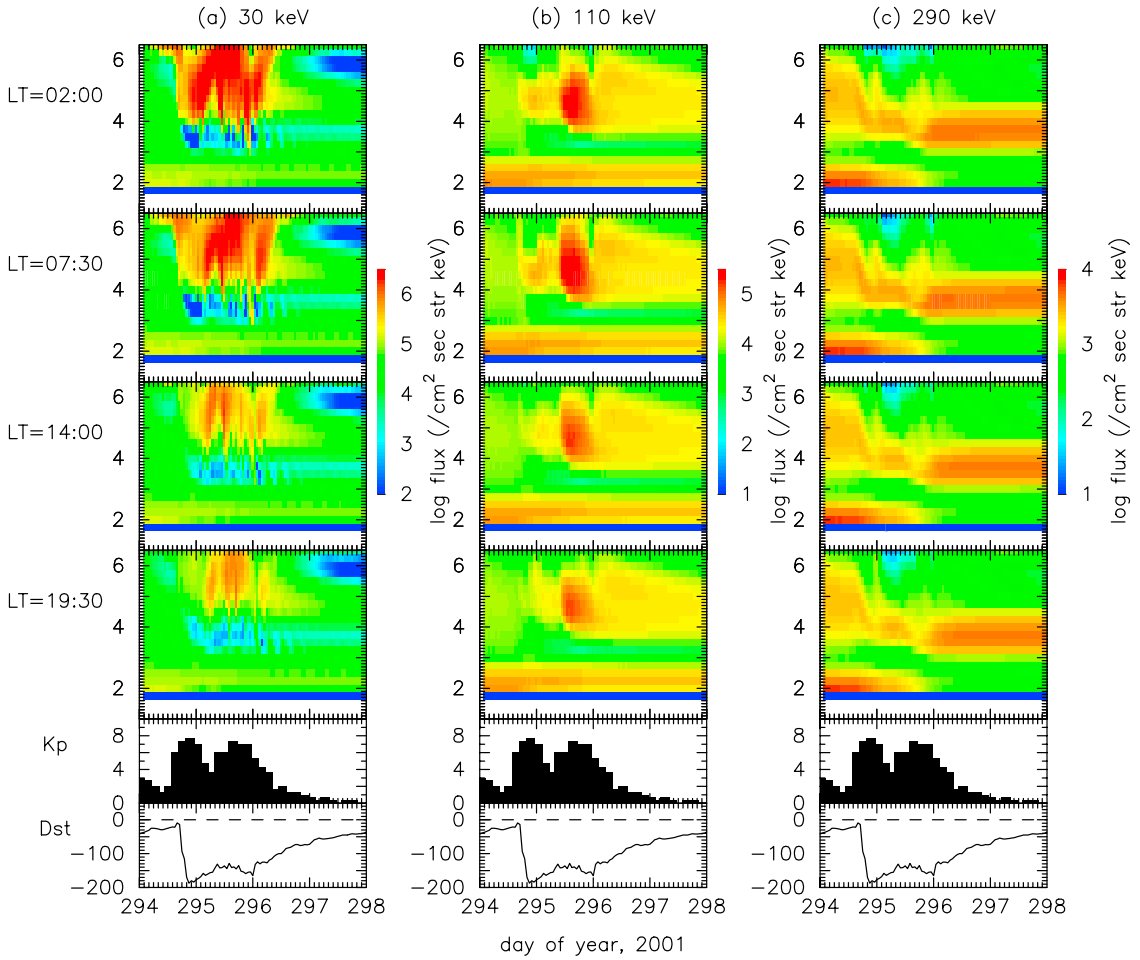

Figure 6. *L*-time diagram of the simulated electron flux of (a) 30 keV, (b) 110 keV, and (c) 290 keV electrons. From top to bottom: MLT of 0200, 0730, 1400, and 1930, respectively.

4.1. Comparison With the NOAA Observations

4.1.1. Main Phase

[25] Figure 6a shows 30 keV electron flux from the simulation. The fluxes of these electrons in the outer region increase at the dawnside and nightside when the convective electric field is enhanced. Following the first flux enhancement, the flux decreases, and then increases again near the second *Dst* minimum. Although these changes are qualitatively similar to the NOAA observations, the observed flux decrease during the first *Dst* minimum is more significant than the simulation. The inner edge of the flux enhancement was below $L = 3$ in the NOAA observations, while the inner edge in the simulation is about $L = 4$. One reason for the discrepancy may be due to inaccurate parameterizations of lifetime, probably underestimation of the life time during the main phase and the period of intense activity. Another reason may be that the Volland-Stern electric field model underestimates the actual electric field in the main phase, limiting the amount of convective transport. In fact, *Rowland and Wygant* [1998] showed that the electric field observed by CRRES is quite larger than the Volland-Stern electric field model during the magnetic disturbed period.

[26] The simulation shows the flux increase at all local times, but the enhancement is much larger at the dawnside and nightside and occurs at larger *L* than at the noonside and duskside. Such local time asymmetry is qualitatively consistent with the observations. *Jordanova and Miyoshi* [2005] concluded that convection is the dominant transport mode of particles in this energy range, and radial diffusion is secondary. This result is also consistent with the simulation study of *Liu et al.* [2003].

[27] Figure 6b shows 110 keV electron flux from the simulation. The flux of these electrons decreases at $L > 5.5$ in the main phase, and then increases at about $L = 5.0$. Such a flux enhancement during the second *Dst* minimum was also seen in the NOAA observations at the nightside and noonside. The simulation shows a dramatic increase of the 110 keV electron flux at $L = 3$–4. The amount of the flux enhancement at the time of the second *Dst* minimum is greater than that in the first *Dst* minimum. As shown by *Jordanova and Miyoshi* [2005], at $L < 4$, radial diffusion is the primary transport mode at this energy range and convective transport is secondary, while at $L > 4$ convection should be more effective.

[28] On the other hand, there are several discrepancies between the simulation and observations. First, the observations show a significant flux enhancement at $L < 3.0$ in the second *Dst* minimum, while the flux enhancement is

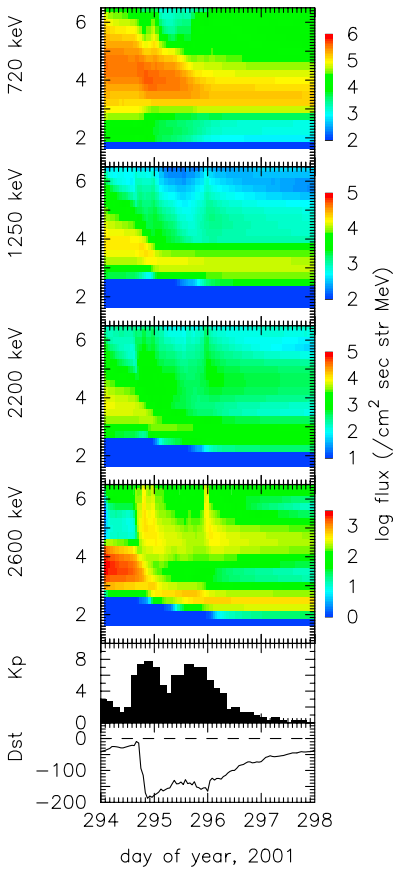

Figure 7. *L*-time diagram of simulated electron flux. From top to bottom: 720 keV, 1250 keV, 2200 keV, and 2600 keV, respectively.

dominant at $L = 4-5$ in the simulation. The position of flux enhancement can be controlled by balance between transport and loss, and further improvements of the diffusion coefficient and life times are necessary to understand the discrepancy between the observation and the simulation. The local source also should be considered in the future study. Second, the observed flux enhancement took place initially in the inner portion of the outer belt, while the simulated flux increases first at the outer portion and then gradually diffuses inward. Third, the observations showed the flux decrease at $L > 4$ during the main phase, while the simulated flux decreases only around $L > 5.5$. The simulation using only convective transport as shown in *Jordanova and Miyoshi* [2005] suggests that the decrease at $L > 5.5$ is mainly due to electrons loss through the dayside magnetopause by convection during the polar cap potential enhancement.

[29] Figure 6c shows the flux of 290 keV electrons from the simulation. The flux of 290 keV electrons decreases at $L > 4.5$ during the main phase. The flux in the outer belt decreases due to enhanced outward radial diffusion prompted by a decrease of the flux at the outer boundary. The result therefore suggests that outward diffusion enhances the main phase dropout of the outer belt. It is noted that the observed flux decrease in the main phase is more significant than the simulation, suggesting that other processes, such as enhanced pitch angle scattering, may contribute to the decrease. The EMIC waves generated by ring current ions are considered to be a plausible candidate for rapid pitch angle scattering of MeV electrons at the duskside [e.g., *Summers and Thorne*, 2003; *Albert*, 2003]. The simulation of EMIC waves from the RAM-ion [*Jordanova et al.*, 2001] shows intense evolution of EMIC waves around the nightside and duskside during the main phase. Pitch angle scattering by EMIC waves may cause electron loss and will be studied in more detail in the future. In addition, magnetic field variations due to ring current evolution can be effective for adiabatic variation of the outer belt electrons [e.g., *Kim and Chan*, 1997] and should affect particles with different energies to different degrees. Although the simulation in this study did not include such a time variations of the ambient magnetic field, that variation may explain a part of discrepancies between the observations and the simulation. Including time-dependent magnetic fields in the simulation is a topic of future work. In the simulation, the flux increase takes place first at $L = 4$ in the main phase and enhances substantially more at $L = 3.5$ in the second *Dst* minimum. The enhanced fluxes diffuse inward from the outer region when radial diffusion is enhanced. The timing of the flux enhancement in the second *Dst* minimum is almost the same as the observations.

4.1.2. Recovery Phase

[30] During the recovery phase, convective transport becomes weak and electrons are no longer injected into the inner magnetosphere because of the absence of substorm activity. As a result, the simulated 30 keV electron flux decreases gradually at $L = 3-5$. Additionally, owing to the decrease of the convective electric field, the particle distribution which was highly asymmetric in local time during the main phase now becomes symmetric in local time. The NOAA observations show these symmetric flux distributions and a gradual flux decrease in the recovery phase.

[31] The simulated fluxes of 110 keV and 290 keV electrons gradually decrease at $L > 3$ during the recovery phase contrary to the NOAA observations which showed the flux increase in the inner region and outward expansion. Moreover, the observed flux enhancement seemed to last from the second *Dst* minimum to the recovery phase. There are no flux enhancements at $L > 4$ in the simulation, except at the outer boundary, because the radial diffusion coefficient is small during the recovery phase. Therefore, the simulation does not well reproduce the enhancement of the higher energy electrons in the recovery phase at large *L*.

4.2. Comparison With the Polar Observations

[32] Taking into consideration the previous results, we compare the simulation results with the Polar observations of MeV electrons. Figure 7 is the *L*-time diagram of the simulation for the same energy range as the Polar observations shown in Figure 5. As mentioned previously, the observed flux below 1293 keV decreased during the main phase and then recovered and increased during the recovery phase. The simulated electron flux in this same energy range shows a different response. During the main phase the simulated 720 keV and 1250 keV electron flux decreases at $L > 5$ and increases at $L = 3-4.5$. In the recovery phase, while the observed fluxes increased, the simulated flux gradually decreases due to pitch angle scattering. The simulated higher energy electron flux also differs from the

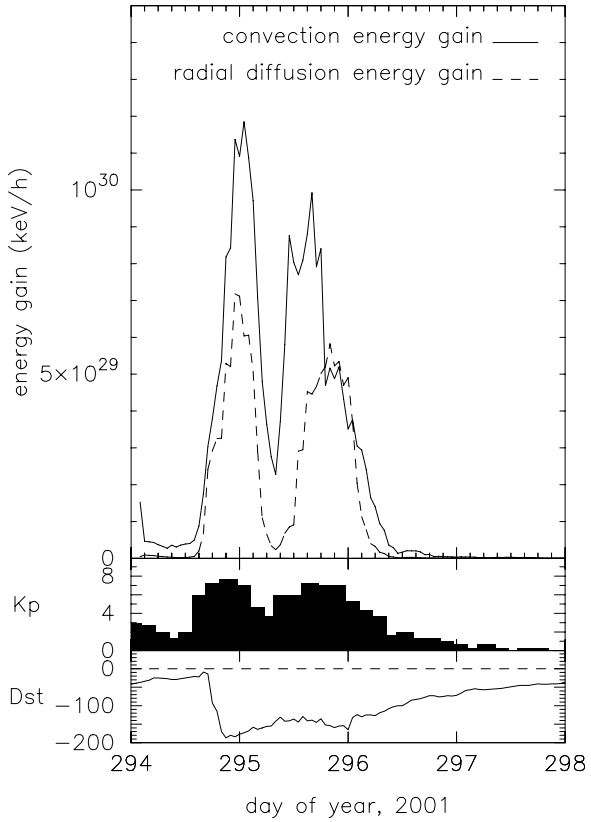

Figure 8. Time profile of energy gain evaluated from the simulation. The solid line is the energy gain from convective transport and the dashed line is the energy gain from radial diffusion.

observations. The 2186 keV electron flux observed by Polar first decreased and then recovered up to, but not above, the prestorm level. The simulated 2200 keV electron flux at $L = 3-5$ decreases after the main phase but never fully recovers to the prestorm levels although there are several very small intermittent flux increases due to diffusion from the outer boundary. The observed 2678 keV electron flux decreased after the main phase and remained low throughout the storm. The simulated 2600 keV electron flux shows some similar variations. That is, the initial flux decreases after the beginning of the main phase. However, similar to the behavior of the 2200 keV electrons, there are several small flux increases due to diffusion from the outer boundary during the main phase and the period of intense activity. Therefore there are some discrepancies between the simulation and the observations for the electrons in the relativistic energy range. The very small flux increases due to diffusion from the outer boundary were not seen by Polar. More noticeably, the simulation does not show any flux enhancements during the recovery phase.

[33] Figure 8 shows the time profile of particle energy gain due to both convection and radial diffusion evaluated from the simulation. The energy gain can be derived from the calculation of the time variation of total energy at each time step. It clearly shows that most of the energization from convection and radial diffusion occurs during the main phase and the period of intense activity while energy gain in the recovery phase is almost negligible. Thus it is expected from the simulation that acceleration and flux enhancement should occur during the main phase and period of intense activity, while the observations indicate that flux enhancement took place in the recovery phase as well. The results suggest that other processes, such as internal acceleration that generates MeV electrons, may explain the discrepancy between the model and the observations. In the present simulation, the energy gain should be small when the *Kp* index is

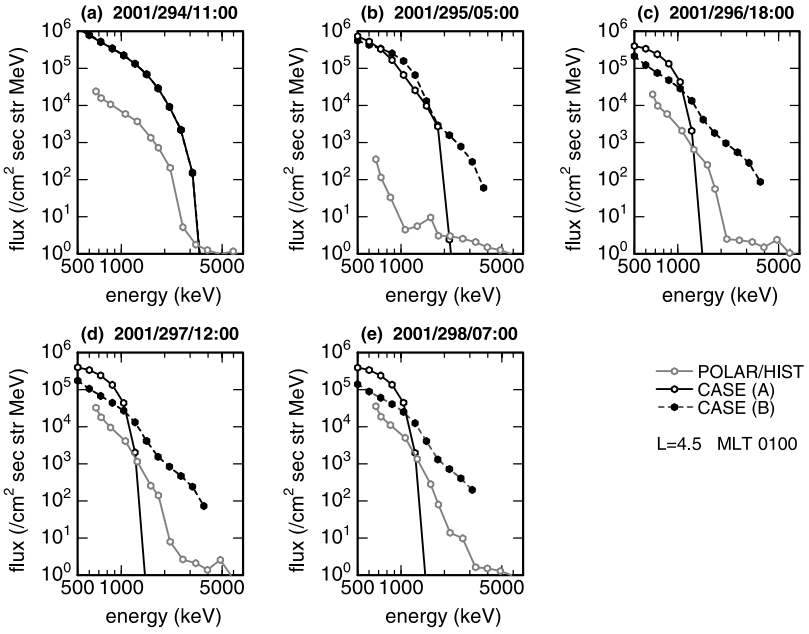

Figure 9. Observed and simulated energy spectrum of electrons above 500 keV at several different periods during the storm. The gray line indicates Polar/HIST measured flux. The line with white circles is the flux from case A simulation and the dashed line with black circle is flux of case B simulation.

small because convection and radial diffusion are scaled by the *Kp* index. Therefore it should be mentioned that there are limits due to the parameterization of the equations. The parameterization tends to produce difference between the model and observations even if the including equations can describe the physics correctly.

[34] Finally, Figure 9 shows the time evolution of the energy spectrum from the Polar observations at $L = 4.5$ compared to two different simulation runs: case A: convection, and case B: convection and radial diffusion. That is, in case A, the radial diffusion process of equation (3) is not included. Figure 9a shows the energy spectrum before the storm commencement. Note that the simulation differs from the observations because the initial distribution of the simulation differs from the Polar observation at these energies. Around the first *Dst* minimum (Figure 9b), the observed flux decreases significantly, while the decreases in the simulation of both cases A and B are not so large. In the MeV energy range, the flux decreases gradually from the period of intense activity to the recovery phase in case A. On the other hand, the energy spectrum in case B hardens in the period of intense activity. Late in the storm, the difference between case A and B is substantial because the flux of MeV electrons decreases in case A, while the energy spectrum in case B maintains a hard spectrum. Polar observed that the flux increases and its energy spectrum continues to slowly harden during the recovery phase, while the flux from case B decreases slowly at all energies maintaining a hard spectrum.

5. Summary

[35] In this paper we compared energetic electron dynamics from several satellites during the October 2001 magnetic storm to the simulations of the evolution of energetic electron flux using the relativistic RAM electron model.

[36] First, we showed the observations of energetic electrons in the inner magnetosphere during the storm. The storm had a long lasting period of the intense geomagnetic activity just after the main phase followed by a very quiet recovery phase. The hot 30–100 keV electron flux increased at $L < 5$ during the main phase and the period of intense activity, while decreasing in the outer region ($L = 5$). In contrast, the higher energy electron flux (300–1200 keV) decreased during the main phase, remained low during the period of intense activity, and then recovered and increased during the recovery phase when the magnetic activity was quiet without any substorms. The flux increase occurred first in the inner region and then expanded outward. Finally, the highest energy electron flux above 1200 keV decreased during the main phase and never fully recovered to prestorm levels.

[37] Next, we simulated this storm and investigated the electron dynamics. The simulated hot electrons (30 keV) moved inward during the main phase and the period of intense activity due to convective transport reproducing the observed local time asymmetry. The 110 keV electrons are subject to convection at $L > 5$ and radial diffusion in the inner region. Thus the flux of 110 keV electrons increased during the main phase and the period of intense activity when these two processes were most intense. The higher-energy electrons (290 keV) were predominantly transported by radial diffusion. The simulation reproduced the flux decrease in the main phase at higher L. The flux increase took place first at $L = 4$ in the main phase and enhanced at $L = 3.5$ at the second *Dst* minimum. The simulated 290 keV electrons gradually decrease in the recovery phase contrary to the NOAA observations. The simulated MeV energy electron flux decreased at $L > 4.5$ in the main phase and never increased in the recovery phase, and this is not consistent with the Polar observations.

[38] The simulation shows that most of the energization via adiabatic transport occurred during the main phase and the period of intense activity, while the observed electron flux enhancements at high energy took place in the recovery phase. The origin of MeV particle energization in the recovery phase of this storm is uncertain and further examination, particularly on plasma waves including both VLF and ULF waves, is necessary.

[39] **Acknowledgments.** We would like to thank R. M. Thorne and J. Albert for useful discussions on this study. The *Dst* and *AE* indices were provided by World Data Center for Geomagnetism, Kyoto, Japan. The *Kp* index was provided by GeoForschungsZentrum Potsdam. The ACE solar wind data and magnetometer data were provided by D. J. McComas and N. Ness, through the Coordinated Data Analysis Web (CDAWeb) at NASA. This work was supported by grant-in-aid for scientific research (17740326) from the Ministry of Education, Science, Sports and Culture, Japan, and by NASA grant NAG5-13512 and NSF grant ATM-0309585.

[40] Arthur Richmond thanks the reviewers for their assistance in evaluating this paper.

References

Abel, B., and R. M. Thorne (1998), Electron scattering loss in Earth's inner magnetosphere: 1. Dominant physical processes, *J. Geophys. Res.*, *103*, 2385.

Albert, J. M. (1999), Analysis of quasi-linear diffusion coefficients, *J. Geophys. Res.*, *104*, 2429.

Albert, J. M. (2003), Evaluation of quasi-linear diffusion coefficients for EMIC waves in a multispecies plasma, *J. Geophys. Res.*, *108*(A6), 1249, doi:10.1029/2002JA009792.

Berg, L. E., and F. Søraas (1972), Observations suggesting weak pitch angle diffusion of protons, *J. Geophys. Res.*, *77*, 34.

Beutier, T., and D. Boscher (1995), A three-dimensional analysis of the electron radiation belt by the Salammbo code, *J. Geophys. Res.*, *100*, 14,853.

Blake, J., et al. (1995), CEPPAD: Comprehensive energetic particle and pitch angle distribution experiment on Polar, *Space Sci. Rev.*, *71*, 531.

Borovsky, J. E., M. F. Thomsen, and D. J. McCormas (1997), The superdense plasma sheet: Plasmaspheric origin, solar wind origin, or ionosphere origin?, *J. Geophys. Res.*, *102*, 22,089.

Bourdarie, S., D. Boscher, T. Beutier, J.-A. Saubaud, and M. Blanc (1997), Electron and proton radiation belt dynamic simulations during storm periods: A new asymmetric convection-diffusion model, *J. Geophys. Res.*, *102*, 17,541.

Brautigam, D. H., and J. M. Albert (2000), Radial diffusion analysis of outer radiation belt electrons during the October 9, 1990, magnetic storm, *J. Geophys. Res.*, *105*, 291.

Chen, M. W., and M. Schulz (2001), Simulations of diffuse aurora with plasma sheet electrons in pitch angle diffusion less than everywhere strong, *J. Geophys. Res.*, *106*, 28,949.

Elkington, S., M. Wiltberger, A. A. Chan, and D. N. Baker (2004), Physical model of the geospace radiation environment, *J. Atmos. Sol. Terr. Phys.*, *66*, 1371.

Evans, D. S., and M. S. Greer (2000), Polar orbiting environmental satellite space environment monitor: 2. Instrument description and archive data documentation, *NOAA Tech. Memo. OAR SEC-93*, Natl. Oceanic and Amos. Admin., Boulder, Colo.

Friedel, R. H., G. D. Reeves, and T. Obara (2002), Relativistic electron dynamics in the inner magnetosphere: A review, *J. Atmos. Sol. Terr. Phys.*, *64*, 265.

Green, J. C., and M. G. Kivelson (2004), Relativistic electrons in the outer radiation belt: Differentiating between acceleration mechanisms, *J. Geophys. Res.*, *109*, A03213, doi:10.1029/2003JA010153.

Horne, R. B., R. M. Thorne, S. A. Glauert, J. M. Albert, N. P. Meredith, and R. R. Anderson (2005), Timescale for radiation belt electron acceleration by whistler mode chorus waves, *J. Geophys. Res.*, *110*, A03225, doi:10.1029/2004JA010811.

Jordanova, V. K., J. U. Kozyra, A. F. Nagy, and G. V. Khazanov (1997), Kinetic model of the ring current-atmosphere interactions, *J. Geophys. Res.*, *102*, 14,279–14,291.

Jordanova, V. K., C. J. Farrugia, R. M. Thorne, G. V. Khazanov, G. D. Reeves, and M. F. Thomsen (2001), Modeling ring current proton precipitation by electromagnetic ion cyclotron waves during the May 14–16, 1997, storm, *J. Geophys. Res.*, *106*, 7.

Jordanova, V. K., and Y. S. Miyoshi (2005), Relativistic model of ring current and radiation belt ions and electrons: Initial results, *Geophys. Res. Lett.*, *32*, L14104, doi:10.1029/2005GL023020.

Kim, H.-J., and A. A. Chan (1997), Fully adiabatic changes in storm time relativistic electron fluxes, *J. Geophys. Res.*, *102*, 22,107.

Li, X. (2004), Variations of 0.7–6.0 MeV electrons at geosynchrnous orbit as a function of solar wind, *Space Weather*, *2*, S03006, doi:10.1029/2003SW000017.

Li, X., M. Temerin, D. N. Baker, G. D. Reeves, and D. Larson (2001), Quantitative prediction of radiation belt electrons at geostationary orbit based on solar wind measurements, *Geophys. Res. Lett.*, *28*, 1887.

Liu, S., M. W. Chen, L. R. Lyons, H. Korth, J. M. Albert, J. L. Roeder, P. C. Anderson, and M. F. Thomsen (2003), Contribution of convective transport to stormtime ring current electron injection, *J. Geophys. Res.*, *108*(AX), 1372, doi:10.1029/2003JA010004.

Lyons, L. R., and M. Schulz (1989), Access of energetic particles to storm time ring current through enhanced radial "diffusion," *J. Geophys. Res.*, *94*, 5491.

Lyons, L. R., and R. M. Thorne (1973), Equilibrium structure of radiation belt electrons, *J. Geophys. Res.*, *78*, 2142.

Lyons, L. R., and D. J. Williams (1984), *Quantitative Aspects of Magnetospheric Physics*, Springer, New York.

Maynard, N. C., and A. J. Chen (1975), Isolated cold plasma regions: Observations and their relation to possible production mechanisms, *J. Geophys. Res.*, *80*, 1009.

Meredith, N. P., R. B. Horne, and R. R. Anderson (2001), Substorm dependence of chorus amplitudes: Implications for the acceleration of electrons to relativistic energies, *J. Geophys. Res.*, *106*, 13,165.

Meredith, N. P., R. B. Horne, R. M. Thorne, D. Summers, and R. R. Anderson (2004), Substorm dependence of plasmaspheric hiss, *J. Geophys. Res.*, *109*, A06209, doi:10.1029/2004JA010387.

Miyoshi, Y., A. Morioka, T. Obara, H. Misawa, T. Nagai, and Y. Kasahara (2003), Rebuilding process of the outer radiation belt during the 3 November 1993 magnetic storm: NOAA and Exos-D observations, *J. Geophys. Res.*, *108*(A1), 1004, doi:10.1029/2001JA007542.

Miyoshi, Y. S., V. K. Jordanova, A. Morioka, and D. S. Evans (2004), Solar cycle variations of the electron radiation belts: Observations and radial diffusion simulation, *Space Weather*, *2*, S10S02, doi:10.1029/2004SW000070.

Naehr, S. M., and F. R. Toffoletto (2005), Radiation belt data assimilation with an extended Kalman filter, *Space Weather*, *3*, S06001, doi:10.1029/2004SW000121.

Obara, T., Y. Miyoshi, and A. Morioka (2001), Large enhancement of the outer belt electrons during magnetic storm, *Earth Planets Space*, *53*, 1163.

O'Brien, T. P., and M. B. Moldwin (2003), Empirical plasmapause models from magnetic indices, *Geophys. Res. Lett.*, *30*(4), 1152, doi:10.1029/2002GL016007.

O'Brien, T. P., K. R. Lorentzen, I. R. Mann, N. P. Meredith, J. B. Blake, J. F. Fennell, M. D. Looper, D. K. Milling, and R. R. Anderson (2003), Energization of relativistic electrons in the presence of ULF power and MeV microbursts: Evidence for dual ULF and VLF acceleration, *J. Geophys. Res.*, *108*(A8), 1329, doi:10.1029/2002JA009784.

Rasmussen, C. E., S. M. Guiter, and S. G. Thomas (1993), A two-dimensional model of the plasmasphere: Refilling time constants, *Planet. Space Sci.*, *41*, 35.

Rowland, D. E., and J. R. Wygant (1998), Dependence of the large-scale, inner magnetospheric electric field on geomagnetic activity, *J. Geophys. Res.*, *103*, 14,959.

Schulz, M. (1991), The magnetosphere, in *Geomagnetism*, vol. 4, edited by J. A. Jacobs, pp. 87–293, Elsevier, New York.

Scudder, J. D., et al. (1995), Hydra-A 3-dimensional electron and ion hot plasma instrument for the Polar spacecraft of the GGS mission, in *The Global Geospace Mission*, edited by C. T. Russell, pp. 459–495, Springer, New York.

Selesnick, R. S., and J. B. Blake (2000), On the source location of radiation belt relativistic electrons, *J. Geophys. Res.*, *105*, 2607.

Selesnick, R. S., J. B. Blake, W. A. Kolansinski, and T. A. Fritz (1997), A quiscent state of 3 to 8 MeV radiation belt electrons, *Geophys. Res. Lett.*, *24*, 1343.

Shprits, Y. Y., and R. M. Thorne (2004), Time-dependent radial diffusion modeling of relativistic electrons with realistic loss rates, *Geophys. Res. Lett.*, *31*, L08805, doi:10.1029/2004GL019591.

Shprits, Y. Y., R. M. Thorne, G. D. Reeves, and R. Friedel (2005), Radial diffusion modeling with empirical lifetimes: Comparison with CRRES observations, *Ann. Geophys.*, *23*, 1467.

Stern, D. P. (1973), A study of the electric field in an open magnetospheric model, *J. Geophys. Res.*, *78*, 7292.

Summers, D., and R. M. Thorne (2003), Relativistic electron pitch-angle scattering by electromagnetic ion cyclotron waves during geomagnetic storms, *J. Geophys. Res.*, *108*(A4), 1143, doi:10.1029/2002JA009489.

Summers, D., R. M. Thorne, and F. Xiao (1998), Relativistic theory of wave–particle resonant diffusion with application to electron acceleration in the magnetosphere, *J. Geophys. Res.*, *103*, 20,487.

Troshichev, O. A., V. G. Andersen, S. Vennerstrom, and E. Friis-Christensen (1988), Magnetic activity in the polar cap -a new index-, *Planet. Space Sci.*, *36*, 1095.

Troshichev, O., H. Hayakawa, A. Matsuoka, T. Mukai, and K. Tsuruda (1996), Cross polar cap diameter and voltage as a function of PC index and interplanetary quantities, *J. Geophys. Res.*, *101*, 13,429.

Vette, J. I. (1991), The AE-8 trapped electron model environment, *NSSDC/WDC-A, 91–24*, Natl. Space Sci. Dat. Cent., Greenbelt, Md.

Volland, H. (1973), A semiempirical model of large-scale magnetospheric electric fields, *J. Geophys. Res.*, *78*, 171.

Zheng, Y., M.-C. Fok, and G. V. Khazanov (2003), A radiation belt-ring current forecasting model, *Space Weather*, *1*(3), 1013, doi:10.1029/2003SW000007.

D. S. Evans and J. C. Green, NOAA, Boulder, CO, USA.

A. Morioka, Planetary Plasma and Atmospheric Research Center, Tohoku University, Sendai, Japan.

Y. S. Miyoshi, Solar-Terrestrial Environment Laboratory, Nagoya University, Nagoya 464-8601, Japan. (miyoshi@stelab.nagoya-u.ac.jp)

V. K. Jordanova, G. D. Reeves, and M. F. Thomsen, Los Alamos National Laboratory, Los Alamos, NM, USA.